On the cause of enhanced landward motion of the overriding plate after a major subduction earthquake

M. D'Acquisto[1], M. W. Herman[1*], R. E. M. Riva[2], R. Govers[1]

[1]Department of Earth Sciences, Utrecht University, Utrecht, the Netherlands
[*]Currently at: Department of Geological Sciences, California State University, Bakersfield, USA
[2]Department of Geoscience & Remote Sensing, Delft University of Technology, Delft, the Netherlands

Key Points:

- Postseismic in-plane bending of the overriding plate enhances landward velocities far from the earthquake
- The modeled landward velocity changes due to bending are smaller, more temporally variable than observed, especially considering afterslip.
- Velocity changes associated with 6 earthquakes indicate slip deficit accumulates faster locally.

Corresponding author: Mario D'Acquisto, `m.dacquisto@uu.nl`

Abstract

Greater landward velocities were recorded after 6 megathrust earthquakes in subduction zone regions adjacent to the ruptured portion. Previous explanations invoked either increased slip deficit accumulation or plate bending during postseismic relaxation, with different implications for seismic hazard. We investigate whether bending can be expected to reproduce this observed enhanced landward motion (ELM). We use 3D quasi-dynamic finite element models with periodic earthquakes. We find that afterslip downdip of the brittle megathrust exclusively produces enhanced trenchward surface motion in the overriding plate. Viscous relaxation produces ELM when a depth limit is imposed on afterslip. This landward motion results primarily from in-plane elastic bending of the overriding plate due to trenchward viscous flow in the mantle wedge near the rupture. Modeled ELM is, however, incompatible with the observations, which are an order of magnitude greater and last longer after the earthquake. Varying mantle viscosity, plate elasticity, maximum afterslip depth, earthquake size, and megathrust locking outside of the rupture does not significantly change this conclusion. The observed ELM consequently appears to reflect faster slip deficit accumulation, implying a greater seismic hazard in lateral segments of the subduction zone.

1 Introduction and Background

The classical view of the earthquake cycle at subduction zones is that slip deficit is regularly accumulated during the interseismic time period and released coseismically in major megathrust earthquakes (e.g., Plafker, 1972; Shimazaki & Nakata, 1980). Geodetic observations of displacement at global navigation satellite system (GNSS) stations indicate that coseismic motion releases slip deficit which accumulated because of interseismic megathrust locking and that the trenchward motion of the overriding plate continues during the postseismic period (e.g., Azúa et al., 2002; Moreno et al., 2011; Loveless & Meade, 2011; Protti et al., 2014). Recent analyses of geodetic observations have shown more complex behavior (Loveless, 2017).

Onshore GNSS stations hundreds of kilometers along-strike away are observed to move landward faster than before the earthquake following 6 recent megathrust events: the 2003 M_W 8.3 Tokachi-oki, 2007 M_W 8.4 Bengkulu, 2010 M_W 8.8 Maule, 2011 M_W 9.1 Tohoku-oki, 2012 M_W 7.4 Oaxaca, and 2014 M_W 8.2 Iquique earthquakes (Heki & Mitsui, 2013; Mavrommatis et al., 2014; Loveless & Meade, 2016; Melnick et al., 2017;

Yuzariyadi & Heki, 2021). The velocities in the period between 4.8 and 6.3 years after the Tokachi-oki earthquake were more landward than before by as much as $\sim 6\ \mathrm{mm \cdot yr^{-1}}$ and at distances of $\sim$ 200–350 km along-trench to the south of the earthquake centroid and $\sim$ 150 km to the northeast (Yuzariyadi & Heki, 2021). Landward velocity increases associated with the Bengkulu earthquake were observed at only one station, located $\sim$ 150 km along-trench from the middle of the rupture. No other GNSS observations were available in its surroundings. The increase was of $5.1\ \mathrm{mm \cdot yr^{-1}}$ when computing post-seismic velocities in the 2.3 years following the earthquake (Yuzariyadi & Heki, 2021). In the 5.5 years after the 2010 Maule earthquake, landward velocities were greater than preseismic values by as much as $\sim 9\ \mathrm{mm \cdot yr^{-1}}$. The increases occurred as close as $\sim$ 500 km along-trench from the middle of the rupture zone (Melnick et al., 2017). Between 0.8 and 3.8 years after the the Tohoku-oki event, the landward velocity increases with respect to preseismic values were as large as $\sim 22\ \mathrm{mm \cdot yr^{-1}}$ and as close as $\sim$ 400 km along-trench from the mainshock centroid (Fig. 1) (Yuzariyadi & Heki, 2021). A landward velocity increase of $4.1\ \mathrm{mm \cdot yr^{-1}}$ was observed between velocities in the 5 years after the Oaxaca earthquake and preseismic velocities (Yuzariyadi & Heki, 2021). This change is observed at a station $\sim$ 150 km along-trench from the middle of the rupture, with no other nearby stations. Landward velocities up to $\sim 4\ \mathrm{mm \cdot yr^{-1}}$ greater than before the event were observed in the 5 years after the Iquique earthquake, at stations $\sim$ 300–400 km along-trench on either side of the rupture centroid (Hoffmann et al., 2018; Yuzariyadi & Heki, 2021). Hoffmann et al. (2018) found landward increases, with respect to preseismic values, as high as $10\ \mathrm{mm \cdot yr^{-1}}$ in the second year after the event.

The landward velocity changes after all six earthquakes show transient behavior, either increasing or decreasing with time, in a period shortly after the earthquake (Yuzariyadi & Heki, 2021). This transient period largely coincides with the previously inferred duration of substantial postseismic transients (particularly afterslip) and lasts $\sim$ 5 years after the Tohoku earthquake and $\sim$ 2 years after the other events. The transient behavior includes changes from trenchward to landward changes in trench-perpendicular velocities within the first 2 years after the Oaxaca (Yuzariyadi & Heki, 2021) and Iquique (Hoffmann et al., 2018) earthquakes. After the transient period, velocity changes do not visibly decay and are constant, except for a moderate increase in the following 3 years after the Iquique earthquake (Yuzariyadi & Heki, 2021).

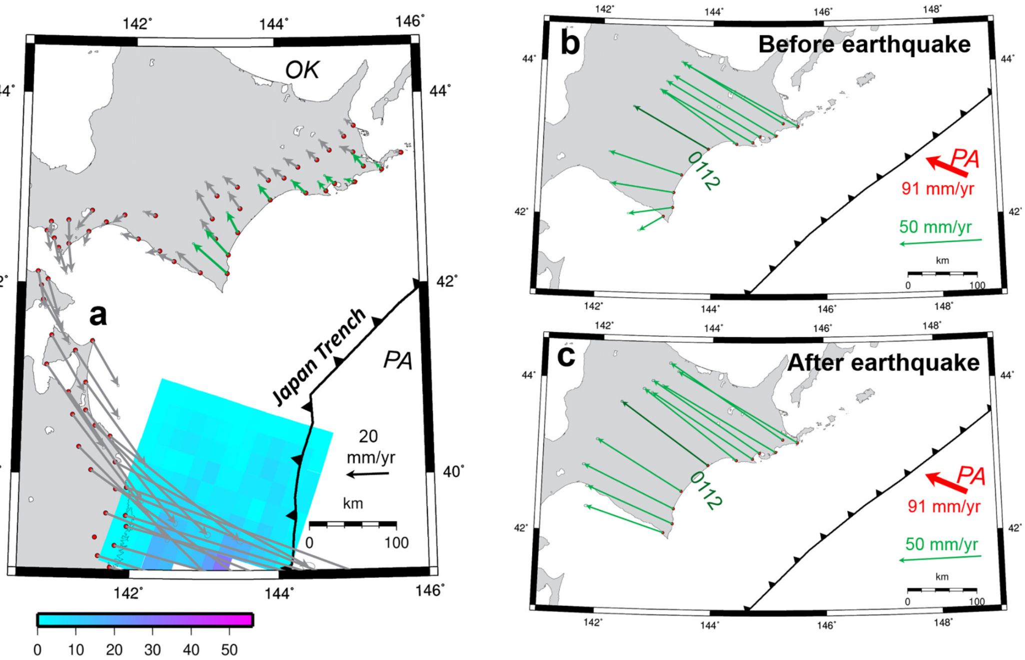

Figure 1. *(a) Horizontal velocity changes, as well as (b) preseismic and (c) postseismic velocities (from the beginning of 2012 to the end of 2014) used to compute them, associated with the 2011 Tohoku earthquake. Cropped from Figure 6 of Yuzariyadi and Heki (2021), used under CC BY (https://creativecommons.org/licenses/by/4.0/)*

An increase of the landward velocity may indicate faster accumulation of slip deficit on locked segments of the megathrust. More generally, it can signify changes in the magnitude or timing of the next earthquake in the area. Melnick et al. (2017) argued that the observed far-field velocity changes do not relate to increased slip deficit accumulation, but could potentially cause temporal clustering of megathrust earthquakes by triggering ruptures of asperities. The 2015 Illapel and 2016 Chiloé earthquakes, which followed the 2010 Maule earthquake in Chile, were interpreted as an example of such clustering (Melnick et al., 2017; Loveless, 2017). This interpretation implies that landward velocity changes may also be responsible for increased shortening rates between clustered historical megathrust earthquakes (Melnick et al., 2017), evidenced for instance by increased subsidence rates recorded by Sumatran microatolls (Meltzner et al., 2015; Philibosian et al., 2014). Ascertaining the mechanism responsible for the landward velocity changes can clarify what changes to seismic hazard should be expected where the changes are observed.

One hypothesis for the acceleration of landward velocities far from a major megathrust earthquake (we will refer to this as "far-field") is an increase in interplate coupling adjacent to the coseismic rupture zone (Loveless & Meade, 2016). The hypothesis stems from kinematic inversions for interplate coupling, in which the higher landward velocities are mapped into increased coupling. This implies that the area of resistive shear tractions on the interface would increase due to a megathrust event hundreds of km away. Another possible explanation for the increased landward velocities is that the subducting slab accelerated as a result of the unlocking of the megathrust in the rupture zone (Heki & Mitsui, 2013). The hypothesis is consistent with marine GPS-acoustic (GPS-A) observations showing increased Pacific plate velocities close to the rupture zone following the 2011 Tohoku-oki earthquake (Tomita et al., 2015). However, slab acceleration due to an altered force balance resulting from the coseismic unlocking of asperities can only occur until the ruptured asperities are relocked. Relocking is inferred to have occurred within a few months to a year after the 2010 Maule, 2011 Tohoku, and other large megathrust earthquakes (Govers et al., 2018). In that case, transient slab acceleration cannot explain average postseismic velocities that are more landward than preseismic velocities over several years. Both increased coupling and slab acceleration require additional postseismic changes to the subduction system other than well-established postseismic processes (e.g., asperity relocking, visco-elastic relaxation, afterslip, poroelastic rebound).

Melnick et al. (2017) proposed a mechanism that would be intrinsic to large megathrust events. In their mechanical models of postseismic deformation following the Maule earthquake, they saw a pattern of velocity changes in the far-field similar to what was observed. The postseismic deformation they modeled also produced stress changes in the neighboring sections of the megathrust, which they identified as the cause of increased seismic activity in those areas, including the 2015 Illapel and, as noted by Loveless (2017), the 2017 Valparaíso earthquake. Melnick et al. (2017) and Loveless (2017) proposed that elastic bending of two plates, in response to postseismic relaxation, causes the far-field landward increases in landward velocities associated with the Maule earthquake. However, they did not compare the amplitude or temporal evolution of the velocity changes resulting from relaxation with the observed ones, nor did they investigate the features of the proposed bending mechanism.

In this paper, we investigate how far-field enhanced landward motion (ELM) may be produced as part of the earthquake cycle, assuming no variations in the megathrust locking pattern or slab acceleration. More specifically, we study under what conditions plate bending driven by postseismic relaxation may occur, and whether the expected acceleration falls within the observed range. As part of this, we aim to establish the sensitivity of this bending mechanism to key features of the megathrust earthquake cycle.

We use numerical models of the earthquake cycle, with physically consistent stresses, strains and slip, to quantify the postseismic deformation field. As far-field accelerated velocities were observed on different subduction margins, we build generic seismic cycle models, not tailored towards any specific margin or megathrust earthquake. In Section 2, we describe our modeling methodology. Our reference model (Section 3.1) shows that postseismic viscous relaxation produces limited ELM, smaller than the cumulative trenchward motion due to afterslip and than the observed ELM. In Section 3.2, we investigate the sensitivity of model results to model parameters. We aim to verify that the observed landward velocities cannot be explained by the model, as well as to find evidence regarding the mechanism by which viscous relaxation produces ELM in the model. We also confirm that locking the lateral portions of the megathrust where viscous relaxation produces ELM does not fundamentally alter the results. In Section 4.1, we use the model results to analyze the mechanism producing ELM in the model. We frame our findings in the context of previous research (Section 4.2) and discuss their implications for seismic hazard (Section 4.3). We summarize our conclusions in Section 5.

2 Numerical Model

We develop three-dimensional mechanical models of the full earthquake cycle. The model geometry involves a realistic slab profile and is uniform in the trench-parallel direction (Fig. 2). Deformation is driven by imposed plate velocities. As the far-field overriding plate is fixed horizontally, all displacements and velocities, both imposed as boundary conditions and resulting from the models, are expressed with respect to the overriding plate. The megathrust is represented by a discrete fault, where earthquakes and afterslip occur in response to accumulated slip deficit. Postseismic relaxation occurs by afterslip and viscous relaxation (Ozawa et al., 2004, 2011; Bürgmann & Dresen, 2008; Diao et al., 2014). We focus on the post-seismic period of repeating earthquake cycles.

2.1 Method

We use a finite element method (FEM) to solve the mechanical equilibrium equations. The massively parallel software package GTECTON (version 2021.0; Govers & Wortel, 1993, 2005; Govers et al., 2018) uses the Portable, Extensible, Toolkit for Scientific Computation (PETSc version 3.10.4; Balay et al., 2021b, 2021a, 1997) and OpenMPI (version 3.0.0 Gabriel et al., 2004). GTECTON provides highly accurate solutions to elastic and visco-elastic problems with arbitrary geometries, a true free surface, and discrete/sharp fault interfaces.

The models have a tetrahedral finite element mesh with a variable resolution, with nodes as little as 4 km apart in high-strain areas close to the edges of the megathrust and asperities. The reference model includes 533,755 nodes and 3,114,252 elements and contains 6000 time steps with a size (Δt) of 1 year, corresponding to 20 earthquake cycles. A visualization of the mesh is shown in Fig. S1. Posterior estimates of the model error (Verfürth, 1994) show that the selected mesh is dense enough to support our conclusion that our results are accurate within a few %.

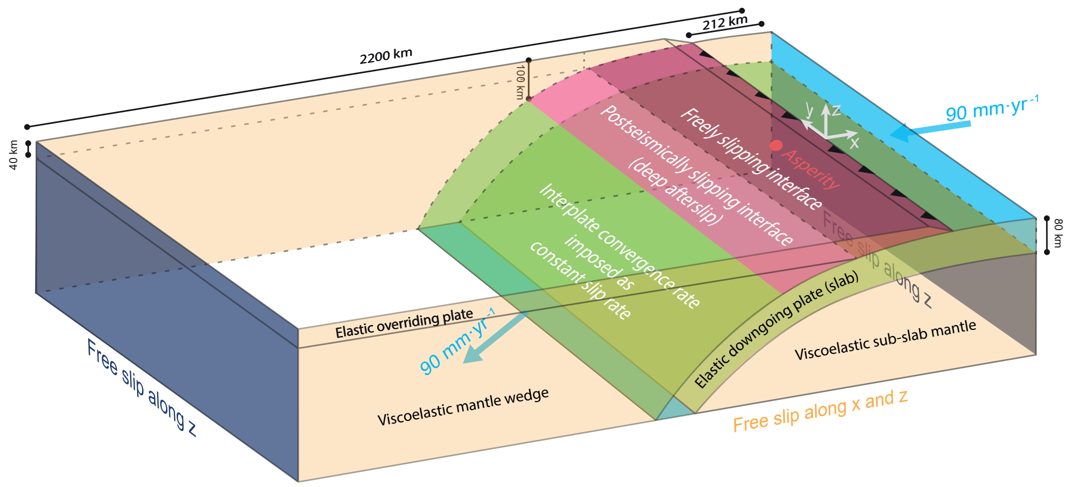

Figure 2. *Model setup geometry, subdomains, boundary conditions and dimensions. The colors on the external surfaces indicate the boundary conditions: light orange—free slip along x and y at the lateral sides; cyan—velocity boundary conditions at the top and bottom of the downgoing plate; dark blue—free slip along z at the landward end). The colors on the top and bottom of the slab distinguish the asperity (red), rest of the brittle megathrust (dark fuchsia), shear zone (bright fuchsia), and interfaces where we impose relative motion at the interplate convergence rate (90* $\mathrm{mm \cdot yr^{-1}}$*).*

Following each coseismic phase and each afterslip phase, 10 consecutive iterations are performed to mechanically re-balance the system. After model spin-up, earthquake cycles are near-identical. There is a difference in surface displacement of less than a few mm between equivalent stages of one cycle and the preceding or following one, while 27 m of interplate convergence occurs over a cycle. We show results from the 19th to 20th cycle.

The models are run in parallel on 10 AMD EPYC 7451 24-core processors with Infiniband, using a Broyden–Fletcher–Goldfarb–Shannon solver (Fletcher, 1988).

2.2 Model Domain and Geometry

The model geometry extends for 2000 km along-trench (in the y direction) and 2200 km in the trench-perpendicular horizontal (x) direction (Fig. 2). The lateral extent of the model domain is chosen so that regions where ELM is expected are not affected by the model edges. We verified that extending the domain further along-trench changes surface motion only minorly and close to the lateral edges. The trench is located at $x =$ 0 and the oceanward model boundary at $x = 212$ km. The positive x direction thus points oceanward. The domain has a vertical extent of 388 km, with z positive upward and $z =$ 0 at the top of the overriding plate. The distance between the trench and the landward edge of the model is 1988 km. We used pilot models to verify that enlarging the domain does not alter the surface deformation of the overriding plate.

The downgoing plate has a thickness of 80 km, consistent with the seismologically detected depth of the lithosphere–asthenosphere boundary of oceanic plates (e.g., Kawakatsu et al., 2009; Kumar & Kawakatsu, 2011), especially for older lithosphere such as on the margins of the Pacific plate (Liu et al., 2017). The top of the downgoing plate follows a trench-perpendicular cross-section through the Slab2 (Hayes et al., 2018) model geometry for the Japan subduction zone, taken to be representative of a typical subduction zone. The overriding plate is 40 km thick with a flat top surface, except for a taper to the trench (at $z = -8$ km) over a horizontal distance (along x) of 18 km.

2.3 Rheology

The model consists of two elastic plates and two asthenospheric domains with isotropic viscoelastic rheological properties. (Fig. 2). The constitutive equations (Govers & Wortel, 2005) are based on compressible elastic deformation and incompressible viscous deformation. Here we use a linear viscosity so that the viscoelastic properties follow a Maxwell model with a characteristic stress relaxation time τ ("Maxwell time"; Appendix A1 in Govers et al. (2018)). Most models have a Young's modulus $E = 100$ GPa and a shear modulus $G = 40$ GPa (corresponding with bulk modulus $K = 66.7$ GPa, compressibility $\beta = 1.5 \cdot 10^{-2}$ GPa^{-1}, and Poisson's ratio $\nu = 0.25$). These elastic parameters are chosen to be consistent with seismological observations (Dziewonski, 1984) as well as spatially uniform, for the sake of simplicity in studying model sensitivity to their value. Below we discuss how a PREM elasticity profile (Dziewonski & Anderson, 1981) affects the results.

The mantle wedge and sub-slab asthenosphere in most of our models have a viscosity $\eta = 10^{19}$ Pa $\cdot$ s. This value is roughly consistent with viscosities determined from observations of postseismic deformation after the 2011 Tohoku-oki (Hu, Bürgmann, Banerjee, et al., 2016) and 2010 Maule (Klein et al., 2016) earthquakes. These viscosity and shear modulus values correspond to a Maxwell time $\tau = \eta/G$ of 7.92 yr (e.g., Spence et al., 1979; Melosh & Raefsky, 1983). In Section 3.2 we investigate the sensitivity of the results to material properties.

2.4 Boundary Conditions

We impose horizontal and trench perpendicular velocity boundary conditions on the oceanic side of the subducting plate (Fig. 2). The rest of this side is allowed to move only in the vertical direction only because we do not model long term convective motions of the asthenosphere. For the same reason, we allow vertical motion only along the vertical continental backside of the model. Slab parallel velocity boundary conditions are imposed where the slab passes through the model bottom boundary. No boundary conditions are applied along the rest of the basal model boundary. We apply free-slip boundary conditions at the lateral sides of the model, i.e., we allow no displacement perpendicular to these boundaries.

Isostatic restoring pressures counteract vertical motions of the free surface of both plates (Govers & Wortel, 1993; ?, ?). These pressures have a magnitude proportional to vertical displacement. The constant of proportionality is the gravitational acceleration

($9.8\ \mathrm{m \cdot s^{-2}}$) times the density contrast ($3250\ \mathrm{kg \cdot m^{-3}}$ at the top of the overriding plate, $2200\ \mathrm{kg \cdot m^{-3}}$ at the top of the oceanic plate).

2.5 The Megathrust

We use the slippery node technique (Melosh & Williams, 1989) to model slip along the megathrust in response to shear tractions that develop in the rest of model. The megathrust is infinitely thin in this formulation, and we impose resistive shear tractions to lock parts of the interface during periods between earthquakes. Herman and Govers (2020) demonstrated that interseismic GPS velocities along the South America subduction margin can be well reproduced using a physical model of fully locked asperities with dimensions of $\approx$ 50 km on a megathrust that can slip freely otherwise. Low shear tractions up- and downdip of seismogenic asperities is consistent with stable sliding at low friction (Hardebeck, 2015; Ikari et al., 2011; Scholz, 1998; Lindsey et al., 2021). Between earthquakes we therefore consider portions of the megathrust as either locked or unlocked.

We use asperities that are circular in map view and that have a diameter of 50 km. In all models, the center of one asperity is located 120 km landward from the trench in the middle of the model (y=0). Some models have additional asperities where landward velocity accelerations may be expected. A model "earthquake" occurs by slip on the megathrust when the central asperity is unlocked, which is imposed to happen every 300 years. Unlocking relaxes all shear tractions on the asperity, and the numerical model finds a solution to the new force balance and stresses using ten iterations. The asperity relocks immediately at the end of the coseismic phase of the model. The moment magnitude of the model earthquake agrees well with the total accumulated slip deficit in and around the asperity.

The rest of the megathrust interface, outside the asperity, can slip freely between earthquakes. However, the continuity of the plates adjacent to the fault results in accumulation of slip deficit within 50km distance of the asperity (Herman et al., 2018). To discourage slip, without preventing it entirely, on the uppermost portion of the megathrust (Kanamori, 1972; Moore & Saffer, 2001; Fujiwara et al., 2011; Sladen & Trevisan, 2018), we apply small shear tractions at depths shallower than 15 km. Their direction is opposite to coseismic slip and their amplitude is directly proportional to it, with a spring constant of $200\ \mathrm{Pa \cdot m^{-1}}$.

2.6 Shear Zone Downdip of the Megathrust

The contact between the mantle wedge and the slab, downdip of the brittle megathrust that releases slip deficit coseismically, hosts slow slip, tremors and low-frequency earthquakes immediately downdip of the rupture area (Behr & Bürgmann, 2020; Lay et al., 2012; Tichelaar & Ruff, 1993). Geodynamic models show that a viscoelastic shear zone develops on geological time scales that facilitates differential motion between the slab and the mantle wedge (van Keken et al., 2002). The maximum depth extent of rapid post-seismic relative motion (afterslip) on the slab-wedge interface is incompletely constrained but is commonly taken to extend to $\sim$ 80–100 km (Diao et al., 2014; Freed et al., 2017; Hu, Bürgmann, Uchida, et al., 2016; Sun et al., 2014; Yamagiwa et al., 2015; Klein et al., 2016) based on post-seismic relaxation observations. We simplify the rheological complexity of the contact zone (Perfettini & Avouac, 2004) by representing it by a thin viscoelastic shear zone with a very low viscosity and with the same elastic properties as the surrounding rocks (Govers et al., 2018; Muto et al., 2019). During the (instantaneous) coseismic motion on the megathrust, there is no differential motion (slip) on the shear zone. Immediately after the coseismic phase,the asperity relocks and very rapid viscous shear stress relaxation occurs in the shear zone. We refer to such rapid postseismic shearing as afterslip. Afterslip is effectively instantaneous in our models. We compute it by rebalancing forces and stresses, using ten iterations, immediately following the coseismic phase, during which no differential motion is allowed on the shear zone downdip of the megathrust. Model afterslip is consequently complete before the onset of bulk viscous relaxation in the wedge and sub-slab asthenosphere (Govers et al., 2018; Muto et al., 2019). The shear zone is represented in the numerical model by an infinitesimally thin interface using slippery nodes (Govers et al., 2018). Additional relative motion occurs on the shear zone during postseismic and interseismic periods as a result of viscous relaxation and continued convergence.

The wedge and slab are modeled as fully coupled beyond the downdip end of the shear zone. In the context of our earthquake cycle models we are not interested in the steady-state convective flow ("corner flow") in the wedge that is driven by slab motion. We therefore use an equivalent of the backslip approach of Savage (1983) along the deeper slab-wedge interface, as follows. The total flow field is the response to both steady subduction and perturbations due to the earthquake cycle. By imposing a steady differential slip rate on the part of the interface where the slab and wedge are fully coupled we isolate the viscoelastic response to the earthquake cycle only. Using the split node technique (Melosh & Raefsky, 1981) we impose a differential slip equal to the imposed subduction rate.

2.7 Slab-Asthenosphere Boundary

We are also uninterested in modeling the steady, long-term, Couette convective flow due to the fact that the slab and underlying asthenosphere are mechanically coupled. We thus isolate the response of the sub-slab asthenosphere to the earthquake cycle. Faulted nodes impose the long term subduction velocity as a backslip rate along the base of the downgoing plate.

2.8 Surface Motion Due To Postseismic Relaxation

Postseismic relaxation in our models involves bulk viscous relaxation and afterslip. Since afterslip is effectively instantaneous in our models, only bulk viscous relaxation produces changes in surface velocities. We compute these velocity changes as $\Delta\vec{v}_{t-\mathrm{pre}} = \vec{v}_t - \vec{v}_{\mathrm{pre}}$, the difference between postseismic velocities $\vec{v}_t$ at time t after the earthquake and the velocities $\vec{v}_{\mathrm{pre}}$ at the last timestep before the earthquake. The latter velocities are taken to represent the near–steady-state contribution of continued convergence with stable coupling at the asperity. When considering cumulative displacement due to both relaxation mechanisms up to a certain time t after the earthquake (Section 3.1.3), we remove the contribution of continued convergence by subtracting $t \cdot \vec{v}_{\mathrm{pre}}$.

Before computing the velocity changes and displacement due to postseismic relaxation, we correct the velocities and displacement for the small effect of deformation due to long-term slab bending and unbending under the applied boundary conditions. The correction is computed by subtracting velocities from an identical model without earthquakes and asperities. Changes in velocities and displacements of the overriding plate thus represent the deformation associated with the earthquake cycle only.

Since the model geometry has reflection symmetry about a trench-perpendicular plane through the middle of the model ($y = 0$), we only plot half of the model ($y \geq 0$) when showing surface velocity or displacements.

3 Results and Analysis

3.1 Reference Model

3.1.1 Model Characteristics

We first present a “reference model”, so called as its parameters and features will be the reference point for the sensitivity study of Section 3.2. The reference model (Ref) has uniform elastic moduli with realistic yet generic values, not aimed at approximating any specific locality: Young’s modulus $E = 100$ GPa and shear modulus $G = 40$ GPa. We use a single, central asperity. This way, we prevent additional asperities and their interseismic, coseismic and post-seismic signals from interfering with the postseismic relaxation that we study. In later models (Section 3.2.5) we discuss the effect of additional coupling in the form of other, laterally located asperities. The asperity is located between 19.5 and 30.2 km depth along the megathrust. Its unlocking causes coseismic slip corresponding to a moment magnitude M_W of 8.9. Afterslip occurs between 40 km (the lower limit of the megathrust interface) and 100 km depth along the slab-wedge interface.

3.1.2 Surface Motion Due to Each Postseismic Relaxation Process

Figure 3(a) shows the cumulative surface displacement due to afterslip on the shear zone separating the slab from the asthenospheric wedge. The trench-perpendicular component of surface displacement of the overriding plate is entirely trenchward (positive). Its amplitude is highest (~ 9 m) between the asperity and the trench and decreases with distance, in both the trench-perpendicular and the trench-parallel directions.

Figure 3(b) shows horizontal velocity changes at time $t = 1$ yr after the earthquake $\left(\Delta\vec{v}_{1\,\mathrm{yr-pre}}\right)$. These velocity changes are landward as close as 700 km along-trench from the middle of the asperity. The maximum amplitude of the landward velocity change occurs around 110 km from the trench and 1054 km from the middle of the asperity (Table 1). The trench-perpendicular gradient in landward velocity changes is small in the offshore, near-trench region (Fig. S2). The velocity changes are highest immediately after the earthquake and decay with time. For instance, the maximum landward velocity change $\left(-\Delta v_{xt-\mathrm{pre}}\right)$ is 0.67 $\mathrm{mm \cdot yr^{-1}}$ at $t = 1$ yr, 0.62 $\mathrm{mm \cdot yr^{-1}}$ at $t = 2$ yr, and 0.58 $\mathrm{mm \cdot yr^{-1}}$ at $t = 3$ yr.

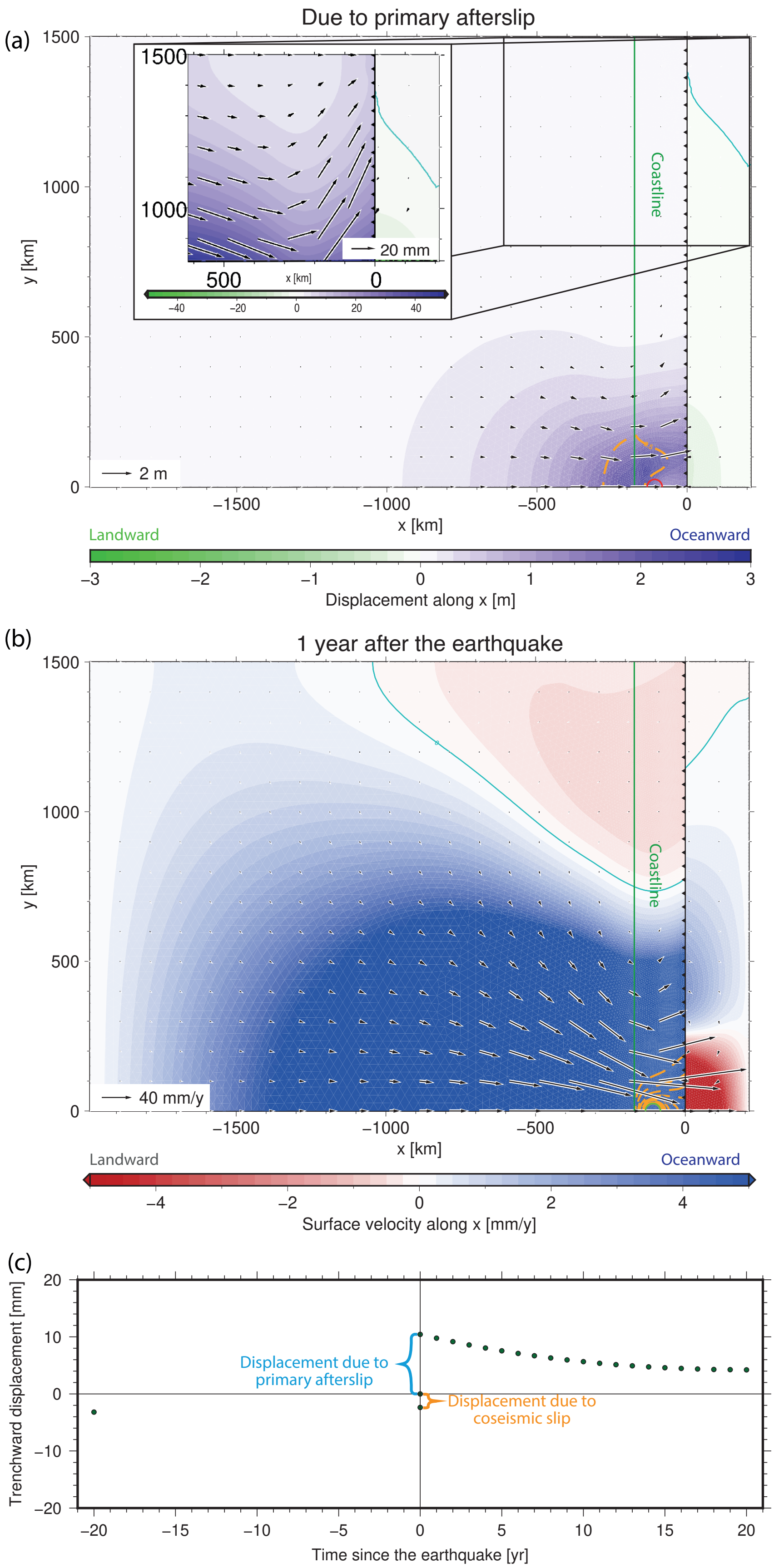
Due to primary afterslip
(a)
y [km]
x [km]
Coastline
2 m
20 mm
Landward
Oceanward
Displacement along x [m]
(b)
1 year after the earthquake
y [km]
x [km]
Coastline
40 mm/y
Landward
Oceanward
Surface velocity along x [mm/y]
(c)
Trenchward displacement [mm]
Displacement due to primary afterslip
Displacement due to coseismic slip
Time since the earthquake [yr]

3.1.3 Cumulative Motion Due to Postseismic Relaxation

Figure 3(c) shows the temporal evolution of trench-perpendicular displacement of one point on the surface of the overriding plate. This point ($x = -170$ km, $y = 1060$ km) is located at the lowest (most landward) $\Delta v_{x\,1\,\mathrm{yr-pre}}$ at the coastline, taken to have the same horizontal location as the downdip end of the megathrust. Displacement is measured as 0 at the end of coseismic slip. Afterslip, instantaneous in the model, produces the trenchward (i.e., positive) displacement at time 0. Landward (i.e., negative) displacement then occurs due to viscous relaxation. At this location, the trenchward displacement due to afterslip is greater than the cumulative ELM due to viscous relaxation at any time. In the 5 years after the earthquakes, the cumulative landward displacement due to viscous relaxation is everywhere smaller than the trenchward displacement due

---

Figure 3 (preceding page). *Horizontal surface motion due to postseismic relaxation in the reference model. (a) Displacement due to afterslip. The color field shows the amplitude of trench-perpendicular displacement (positive landward), while the vectors show the direction and magnitude of horizontal displacement, including the trench-parallel component. In the cutout, the color scale is clipped at 50 mm to show the displacement in the far-field along-trench region. The cyan contour marks 0 trench-perpendicular displacement, separating landward from oceanward motion. The black barbed line shows the location of the trench. The outline of the asperity is shown in red. The dashed orange lines are 2.5 m contours of slip on the shear zone and megathrust due to afterslip. The approximate location of the coastline, taken to be directly above the downdip limit of the locked asperity, is shown in green. Only half the model is shown because of symmetry about the middle ($y = 0$). (b) Velocity changes (postseismic minus pre-seismic), 1 year after the earthquake, due to viscous relaxation. The color field shows the amplitude of trench-perpendicular velocity, while the vectors show the direction and magnitude of horizontal velocity. The color scale is clipped at* $\pm 5\ \mathrm{mm \cdot yr^{-1}}$ *to show landward velocity changes. The cyan contour marks 0 trench-perpendicular velocity. The black barbed line shows the location of the trench. The outline of the asperity is shown in green. The dashed orange lines are 2.5 m contours of coseismic slip on the megathrust. The approximate location of the coastline is shown in green. Only half the model is shown. (c) Temporal evolution of total trench-perpendicular surface displacement (dots) at one point in the model ($x = -170$ km, $y = 1060$ km), minus the contribution of the velocity at the end of the interseismic stage, beginning immediately after the coseismic stage.*

to afterslip. We expect the viscosity of the asthenosphere to control the rate at which viscous relaxation occurs and thus the temporal evolution of the resulting landward displacement. We later explore the effect of different viscosities (Section 3.2.3).

3.2 Sensitivity Testing

3.2.1 Maximum Depth Extent of Afterslip

We evaluate the sensitivity of our model results by varying the maximum depth at which the relative motion between the slab and mantle wedge can deviate from the interplate convergence rate. This restricts afterslip and associated slip deficit accumulation on the deep shear zone. This parameter is the major mechanical constraint on material deformation, for a given rheological structure and megathrust locking pattern.

First, we restrict afterslip to moderate depths, shallower than 75 km (model Aft75). The maximum landward velocity change 1 year after the earthquake is slightly lower than that produced in the reference model with a maximum afterslip depth of 100 km (Table 1). Landward velocity changes also occur ~ 50 km along-trench closer to the middle of the asperity. We then restrict afterslip on the shear zone (downdip of the megathrust and thus deeper than 40 km) to very shallow depths, less than 45 km (model Aft45). The landward displacement due to afterslip is greatly reduced, but so is the maximum landward velocity change due to viscous relaxation (Table 1 and Figs. 4 and S3). Next, we allow afterslip to occur at greater depths, as much as 150 km (model Aft150). Compared to the reference model, the landward velocity changes at time $t = 1$ y after the earthquake have a near-identical maximum amplitude, occurring next to the trench and at a greater along-trench distance from the middle of the asperity (Table 1). Lastly, we completely remove any restriction on afterslip, allowing the relative velocity of the mantle wedge and slab to vary at any depth in response to postseismic deformation (model AllAft). Removing the restriction on afterslip completely eliminates any landward velocity changes due to viscous relaxation.In our models, not allowing time-variable slip rates in the deep shear zone is necessary for enhanced landward velocities to result from postseismic viscous relaxation. The spatial extent of this restriction determines the specific pattern of velocity changes produced.

To better understand the mechanism responsible for ELM generation in our models, we further investigate the relationship between the restriction of motion and the pro-

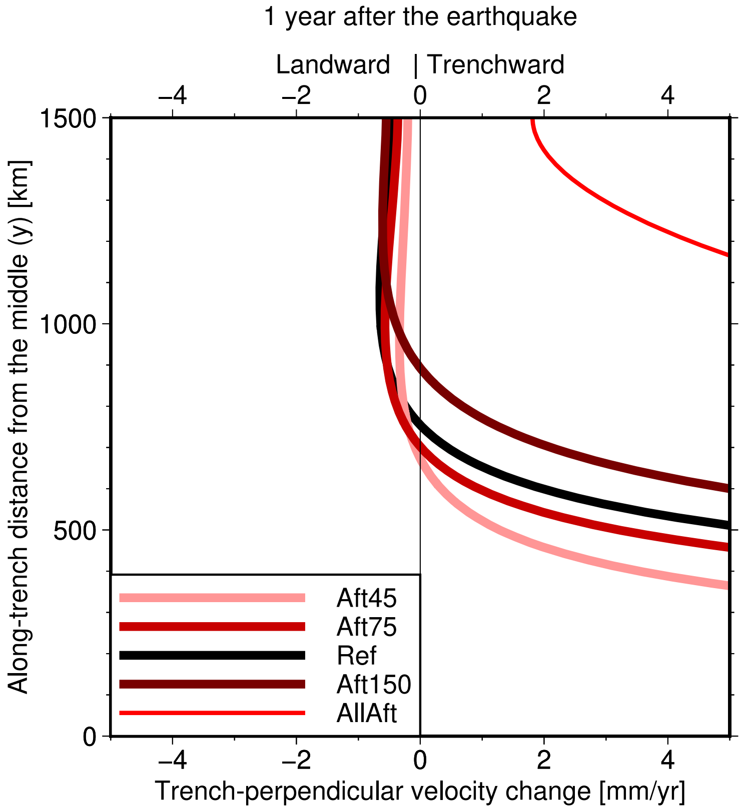

Figure 4. *Sensitivity to different limits to afterslip on the shear zone downdip of the megathrust of trench-perpendicular surface velocity change 1 year after the earthquake along trench-parallel profiles 170 km from the trench.*

duction of ELM by viscous relaxation. We take the model with no limits on afterslip (AllAft) and we introduce a backstop in the overriding plate. We do this by imposing no trench-perpendicular displacement, at all depths within the plate, at a horizontal distance of 400 km from the trench. This model (AllAftB1) produces landward surface velocity changes due to postseismic viscous relaxation (Table 1). The far-field portion of the plate has an opposite pattern of trench-perpendicular motion, with landward velocity changes in the central part of the model and lower trenchward velocities farther along-trench. Increasing the horizontal distance from the trench to the free-slip boundary to 700 km (model AllAftB2) decreases the maximum landward velocity change 1 year after the earthquake and increases the minimum along-trench distance from the middle to landward velocity changes at that time.

Table 1. *Main features of landward velocity changes due to viscous relaxation 1 year after the earthquake in different models*

Model name	Model description	Maximum landward $\Delta v_{x\,1\mathrm{yr-pre}}$ ($\mathrm{mm \cdot yr^{-1}}$)	Location (x, y) of maximum landward $\Delta v_{x\,1\mathrm{yr-pre}}$ (km)	Minimum y of landward $\Delta v_{x\,1\,\mathrm{yr-pre}}$ (km) at $x = -170$ km
Ref	Reference model	0.7	$(-110, 1054)$	736
Aft45	Afterslip above 45 km depth	0.3	$(-230, 975)$	975
Aft75	Afterslip above 75 km depth	0.6	$(-138, 995)$	681
Aft150	Afterslip above 150 km depth	0.7	$(-6, 1241)$	879
AllAft	No lower limit to afterslip	0	N/A	N/A
LoEta1	$\eta = 2 \cdot 10^{18}$ Pa · s (both mantles)	2.4	$(-171, 1121)$	806
LoEta2	$\eta = 2 \cdot 10^{18}$ Pa · s (wedge only)	3.6	$(-118, -880)$	897
HiEta1	$\eta = 5 \cdot 10^{19}$ Pa · s (both mantles)	0.1	$(-105, 1051)$	729
HiEta2	$\eta = 5 \cdot 10^{19}$ Pa · s (wedge only)	0.1	$(-430, 1500)$	1125
LoErefK	$E = 20$ GPa, Ref K (ov. plate)	5.6	$(-82, 409)$	295
RefEloK	$K = 33.3$ GPa, Ref E (ov. plate)	0.7	$(-58, 1149)$	834
E30-150	$E = 30$ GPa ($\lvert x \rvert < 700$ km), 150 GPa ($\lvert x \rvert > 700$ km) (ov. plate)	2.2	$(-74, 514)$	397
LatAsp	Lateral asperities present	0.6	$(-61, 1500)$	646
AllAftB1	AllAft with no x-displacement in overriding plate at $x = 400$ km	10.5	$(-106, 460)$	300
AllAftB2	AllAft with no x-displacement in overriding plate at $x = 700$ km	5.8	$(-85, 870)$	570

3.2.2 Earthquake Magnitude

We examine the robustness of our results when the size of the earthquake changes. To this end, we reduce the interplate convergence rate, uniformly lowering the slip deficit accumulated and released over an earthquake cycle without varying its spatial pattern. Halving the convergence rate, and thus the seismic moment M_0, reduces the moment magnitude M_W from 8.92 to 8.71 and halves the displacement due to afterslip and the velocity changes due to viscous relaxation at any time. Similarly, reducing M_0 by an order of magnitude (and M_W from to 8.25) also reduces the velocity changes and displacement to a tenth. Therefore, with a given interplate locking pattern, ELM produced by postseismic relaxation scales linearly with seismic moment M_0. This is unsurprising, given the linear nature of the rheologies used in the model. Given the amplitude of the ELM in the reference model, even an earthquake larger than any ever recorded would produce smaller landward velocity changes than the largest values observed.

3.2.3 Mantle Viscosity

Mantle viscosity controls the rate of viscous relaxation, which produces enhanced landward velocity changes in our reference model. We alter the viscosity η, and thus the Maxwell relaxation time τ, to investigate its effect on our findings. First, in model LoEta1 we decrease η and τ in both the asthenospheric wedge and sub-slab asthenosphere by a factor of 5 compared to reference values, to $2 \cdot 10^{18}$ Pa $\cdot$ s and ~ 1.59 years, respectively. We decrease the timestep size by the same factor of 5 to accurately resolve the displacement. The earthquake size ($M_W = 8.91$) and recurrence interval ($T = 300$ years) are unaltered. The resulting landward velocity changes are dramatically higher than in the model with reference rheology and earthquake size and a single asperity (Table 1 and Figs. S4 and 5a). However, the maximum amplitudes of the landward velocity changes are still smaller than observed (Section 1 Yuzariyadi & Heki, 2021). The velocity changes decay faster than with the reference viscosity, with the peak amplitude going from 2.5 mm $\cdot$ yr^{-1} at $t = 1$ year to 1.6 mm $\cdot$ yr^{-1} at $t = 2$ years. In a related experiment (LoEta2), we decrease the viscosity compared to the reference model to $2 \cdot 10^{18}$ Pa $\cdot$ s in the mantle wedge only, keeping it at 10^{19} Pa $\cdot$ s in the sub-slab mantle. The maximum landward velocity change after 1 year is more than 50% higher than in LoEta1 (Table 1 and Figs. S4 and 5b). However, these velocity changes are still lower than observed after the Tohoku-oki, Tokachi-oki and Maule earthquakes (Yuzariyadi & Heki, 2021). Also, the model velocities decay rapidly, having a maximum amplitude of 3.8 mm $\cdot$ yr^{-1} at $t = 1$ year and 2.0 mm $\cdot$ yr^{-1} at $t = 2$ years. The greater landward velocity changes due to viscous relaxation when the viscosity is lower in the mantle wedge only indicate that they are driven by viscous flow in the wedge itself, while flow in the sub-slab mantle opposes them.

Since the earthquake size and elastic properties have not changed, afterslip and the surface motion it causes, via elastic deformation, are the same as in the reference model. The displacement due to the instantaneous afterslip in the model is entirely trenchward. In reality, afterslip has a finite, relatively short duration (a few years following the Tohoku earthquake, for instance, per Muto et al., 2019; Yamagiwa et al., 2015). We compare the cumulative surface displacement due to bulk viscous relaxation in the 2 years after the earthquake (and thus after the instantaneous afterslip) with that due to the afterslip. The landward motion due to viscous relaxation does exceed the trenchward motion due to afterslip, in the along-trench far-field portions of the overriding plate, but by a very limited amount, only as high as ~ 1.0 mm.

Increasing the viscosity of both asthenospheric domains by a factor of 5 to $5{\cdot}10^{19}$ Pa $\cdot$ s (model HiEta1), decreases the maximum landward amplitude of velocity changes 1 year after the earthquake (Table 1 and Figs. S5 and 5a). It also decreases the rate of decay with time of the velocity changes. For instance, the maximum landward amplitude after 10 years (0.12 mm $\cdot$ yr^{-1}) is only 11.5% lower than after 1 year. Increasing the viscosity only in the mantle wedge has a small effect on the maximum landward velocity change at any time (Table 1 and Figs. S5 and 5b). However, it varies the spatial pattern of the velocity changes significantly, pushing the peak landward value far from the trench and at the lateral edge of the model ($y = 1500$ km). This occurs because the relatively small contribution of sub-slab viscous relaxation to surface velocities on the overriding plate is increased.

We have shown how the viscosity of the mantle wedge controls the amplitude and temporal decay of the landward velocity changes. A low viscosity produces large velocity changes, which can even compensate for the trenchward motion due to afterslip and produce net ELM. However, the velocity changes decay rapidly with time as viscous relaxation proceeds and are much smaller already a few years after the earthquake. Higher viscosities produce long-lasting velocity changes due to viscous relaxation, but their amplitudes are very small. Furthermore, the occurrence of afterslip should lead to consis-

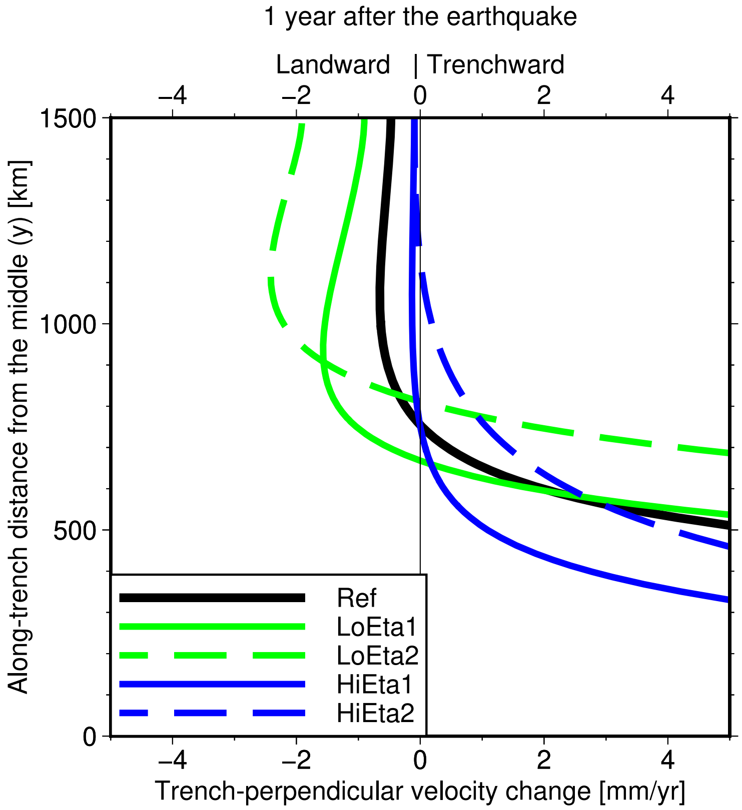

Figure 5. *Sensitivity to different mantle viscosities of trench-perpendicular surface velocity change 1 year after the earthquake along trench-parallel profiles 170 km from the trench.*

tently landward average velocity changes in the months and years after the earthquake during which deep afterslip is occurring. In contrast, velocity changes have been observed to transition from trenchward to landward only after two earthquakes (Iquique and Oaxaca) and within the first year after the event (Yuzariyadi & Heki, 2021; Hoffmann et al., 2018).

3.2.4 Elastic Moduli and Compliance Contrast

We test the sensitivity of our reference model results to changing the elastic parameters of the overriding plate, where the enhanced landward velocities are observed. The effect on modeled ELM of varying the parameters within the realistic range for Earth materials is limited. Furthermore, tailoring the values and spatial distribution of model parameters realistically for specific settings and scenarios is outside the scope of this study. We thus vary the parameters uniformly, choosing extreme values to highlight their effect on ELM and help us investigate the mechanism that produces it. In model LoErefK, we reduce Young's modulus E by a factor of 5, from 100 to 20 GPa, and the shear modulus G from 40 to 6.9 GPa, without changing the bulk modulus K (66.7 GPa) and thus the compressibility $\beta = \frac{1}{K}$ $(1.5 \cdot 10^{-11}\ \mathrm{Pa}^{-1})$. This increases Poisson's ratio from to 0.25 to 0.45, close to its uppermost possible value of 0.5. The resulting landward velocity changes are considerably greater and closer to the asperity than in the reference model (Table 1 and Fig. S6a).

In a related but different experiment (RefEloK), we keep the reference E, bring ν to 0 (as low as possible while not negative) and halve K from 66.7 to 33.3 GPa. β is then twice as large ($3.0 \cdot 10^{-11}$ Pa^{-1} instead of $1.5 \cdot 10^{-11}$) and G is 50 GPa. The resulting velocity changes 1 year after the earthquake have a very similar maximum amplitude as the reference model, although with a different pattern (Table 1 and Fig. S6b). In particular, the maximum landward velocity change is closer to the trench but farther from the asperity. The minimum along-trench distance from the middle to the landward velocity changes is greater than in the reference model. The ELM produced by viscous relaxation, when trench-perpendicular displacement is restricted at a certain distance from the trench, is primarily due to the elastic stiffness G of the overriding plate.

We then introduce a contrast in elastic stiffness between the overriding plate within a few hundred km of the trench and the plate farther inland. This represents the contrast between the hot, intensely deformed, tectonically young arc and backarc region, trenchward of the contrast, and the more stable interior of the overriding plate, landward of the contrast. This contrast produces a steep decrease in trench-perpendicular interseismic velocities with distance from the trench in the first few hundred km adjacent to the coast, at the location of the locked asperity, compatibly with observations (e.g., Chlieh et al., 2008; Ruegg et al., 2009; Loveless & Meade, 2010; Métois et al., 2012; Weiss et al., 2016). We use values of Young's modulus E (150 GPa) and shear modulus G (60 GPa) five times greater at horizontal distances from the trench beyond 700 km than closer to the trench (where they are 30 and 12 GPa, respectively). This is roughly the minimum ratio of the contrast that produces a noticeable break in the trench-perpendicular gradient of interseismic velocities and allows for the use of elastic moduli near the bottom and top of the range of realistic values for consolidated rock materials (D'Acquisto et., submitted). The surface velocity changes 1 year after the earthquake, have a maximum amplitude of $\sim 2.2\ \mathrm{mm} \cdot \mathrm{yr}^{-1}$ (Table 1 and Figs. S7 and 6). This is considerably more

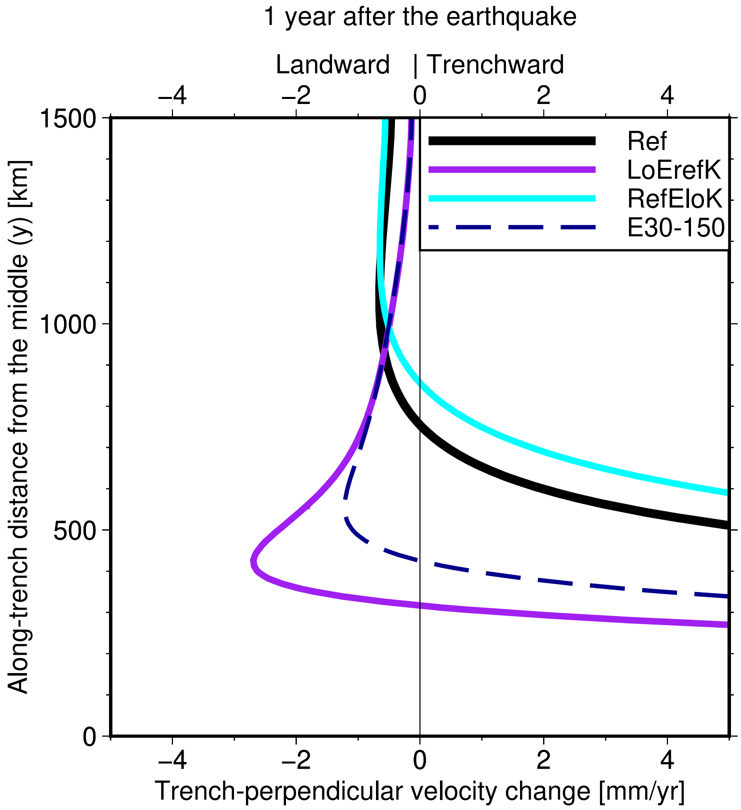

Figure 6. *Trench-perpendicular surface velocity change 1 year after the earthquake along trench-parallel profiles 170 km from the trench ($x = -170$ km) for different overriding plate elastic moduli.*

than in the reference model, but still less than the observed landward velocity changes (Yuzariyadi & Heki, 2021, see Section 1), despite the model earthquake having a greater magnitude than all observed events but Tohoku-oki. The peak landward velocity change at that time is located ~ 520 km along-trench from the middle of the asperity, while the shortest distance from the middle to landward velocity changes then is ~ 400 km. Primary afterslip still produces substantial displacement there (several tens of mm), causing the average cumulative velocity changes from both afterslip and viscous relaxation to be entirely landward over any length of time after the earthquake.

3.2.5 Adjacent Megathrust Locking

Our previously presented models have a single locked asperity on the megathrust.The observed lateral velocity changes, however, occur in areas with non-zero preseismic landward velocities and thus inferred interplate locking (Yuzariyadi & Heki, 2021; Loveless & Meade, 2016). Therefore, in the LatAsp model we test the effect of locking the megathrust along most of its along-trench extent. Starting with the reference model, we add two intermediate lateral asperities extending from 150 to 650 km along-trench from the middle and two external lateral asperities extending from 800 to 1300 km along-trench. All lateral asperities are identical to each other and ellipsoidal in map view. Their trench-perpendicular horizontal width (50 km) and distance from the trench (centered 120 km away) are the same as for the middle asperity. All asperities need to be periodically unlocked and relocked for the model to have multiple earthquake cycle and thus develop background stresses. We use the same recurrence interval of 300 years for each asperity, and thus for the resulting earthquake supercycle. We unlock the first set of additional asperities 20 years after the middle asperity and the second set after 20 more years. We look at the landward velocity changes due to viscous relaxation after the earthquake on the middle asperity. The amplitude of velocity changes directly above the most external asperities and trenchward of them is decreased, compared to the reference model, to less than 0.5 $\mathrm{mm} \cdot \mathrm{yr}^{-1}$ (Fig. S8). The maximum landward amplitude is decreasedand shifted farther from the middle(Table 1 and Fig. 7). The overall area occupied by landward velocity changes is very similar, although it locally stretches closer to the middle of the central asperity. Overall, adding additional locked asperities on the lateral portions of the megathrust modifies the specifics of the ELM produced by postseismic viscous relaxation, without fundamentally altering it.

4 Discussion

4.1 The Mechanism Behind Enhanced Landward Velocity in Our Models

Our results show that restricting the maximum depth of afterslip is needed for ELM to be produced during viscous relaxation. Changing this depth affects the resulting ELM pattern, as does introducing a trench-parallel contrast in overriding plate compliance. These sensitivites suggest that the mechanism producing the ELM relies on restricting trench-perpendicular motion.

We further our understanding of the mechanism responsible for ELM due to viscous flow by analyzing the mechanical response of an elastic plate to trenchward trac-

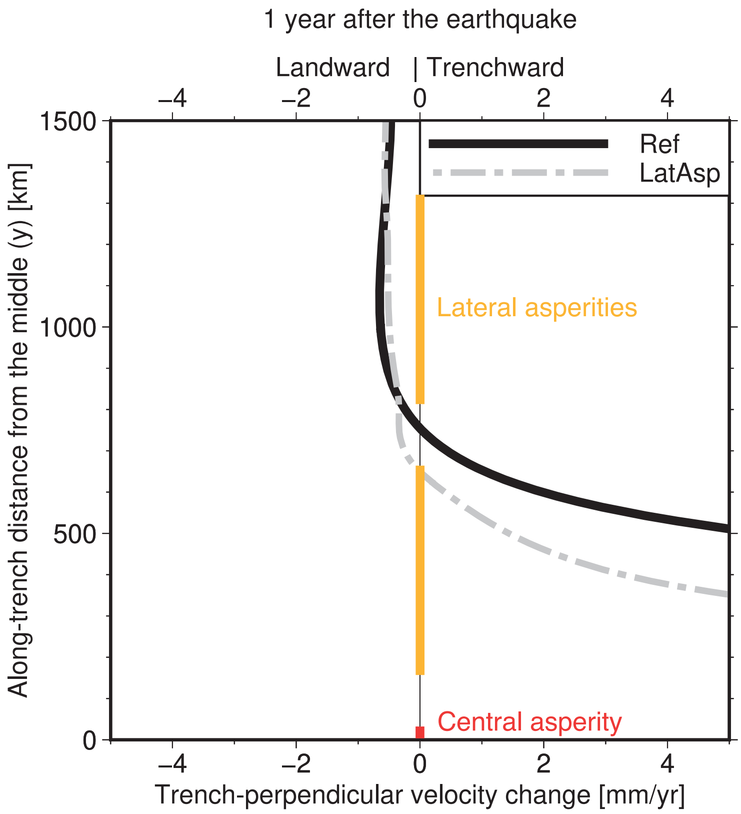

Figure 7. *Sensitivity to different megathrust locking patterns of trench-perpendicular surface velocity change 1 year after the earthquake along trench-parallel profiles 170 km from the trench. The colored lines on the vertical axis mark the along-trench spatial extent of the asperities.*

tions, such as those applied to the overriding plate by viscous relaxation in the mantle wedge. Analytical models show in-plane bending of an semi-infinite elastic plate in response to a horizontal pull force on the free lateral side of the plate (Landau et al., 1986, chapter 13). In the context of an elastic overriding plate the free side would be the trench and the force would result from a traction along the megathrust. Only if displacements are imposed to be zero at some distance from the trench, the analytical solution shows seaward displacement of the trench where the force is applied, and landward displacement of the trench further away from it. Although this result is very interesting, it is of limited direct use to ELM because of simplifications in the model setup. We thus explore a two-dimensional (2D) numerical model to identify the nature of the tractions that drive ELM.

The 2D model includes only a plate with a uniform thickness of 40 km and the same rheological parameters as in our reference earthquake cycle model. We ignore vertical motion and variation of horizontal motion with depth by using a plane-stress approximation (Govers & Meijer, 2001). We apply a free-slip boundary condition to the lateral and landward edges, while the trenchward edge is left free. A trenchward traction applied on a square patch at the bottom of the plate represents the trenchward tractions due to viscous relaxation in the mantle wedge in the vicinity of the rupture. In response to the traction and boundary conditions, the plate moves trenchward in the middle, but landward laterally. The trench-perpendicular width of the plate determines the location of the trenchward displacement. This suggests that the ELM produced by viscous relaxation in the earthquake cycle model is due to the fundamental in-plane elastic response to the trenchward flow that occurs in the mantle wedge during such relaxation.

Figure 8 summarizes our understanding of the deformation mechanism that results in ELM due to viscous relaxation. Trenchward viscous flow in the mantle wedge applies a trenchward horizontal traction rate on the base of the overriding plate. The downdip limit of afterslip prevents the shear zone to slip, in the downdip direction, at rates different than the interplate convergence rate, beyond a certain distance from the trench. This restricts trench-perpendicular velocity changes in the overriding plate, which is mechanically coupled to the wedge. The elastic in-plane response to a trenchward traction of the narrow region of a plate comprised between the trench and the horizontal location of the downdip limit of variable shear zone slip produces a rotational pattern of surface motion with limited landward motion on the sides. The location of the limit of af-

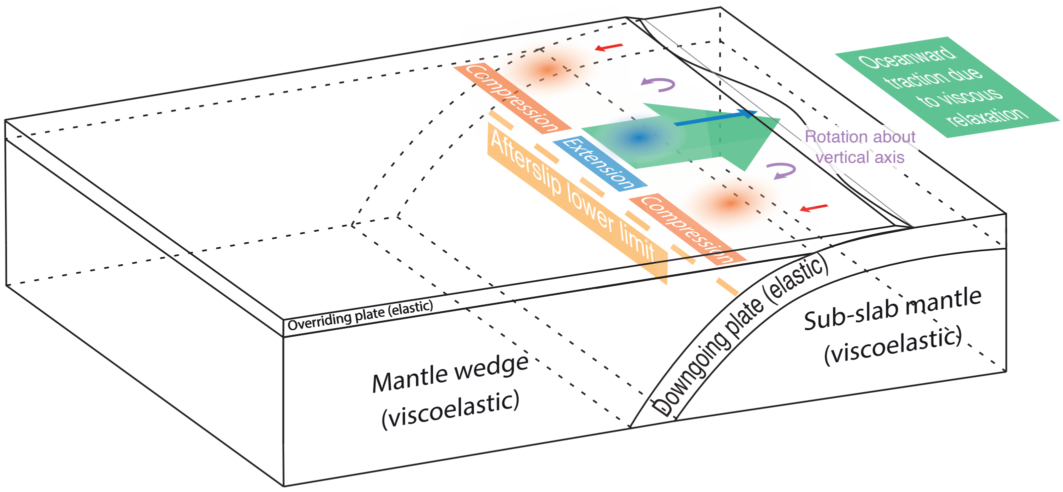

Figure 8. *Mechanism responsible for ELM during viscous postseismic relaxation: trenchward traction rates on the base of the overriding plate, resulting from postseismic visco-elastic mantle flow, cause elastic in-plane bending of the overriding plate, with rotation about a vertical axis. When there is a downdip limit to afterslip, the bending produces enhanced landward displacement to the sides of the ruptured asperity.*

terslip determines the resulting pattern of motion, given a certain rheology and asperity size and slip deficit. Without any restriction on afterslip, the wavelength of the possible bending is such that the entire overriding plate moves trenchwards.

Our sensitivity study shows that the landward velocity changes depend more on the elastic stiffness of the plate (when the compressibility is kept constant) than on its compressibility (while the shear modulus is kept constant). This suggests that bending of the plate is the governing mechanism producing such motion, rather than compression—determined by the finite compressibility—in response to extension near the asperity. The compressibility does modulate the spatial pattern of velocity changes, but is less important in determining their amplitude and location.

4.2 Consistency With Previous Research

4.2.1 Plate Bending Due to Postseismic Relaxation

Our results indicate that viscous relaxation following a megathrust earthquake can, by itself, produce ELM as part of a rotational pattern of velocity changes. This is consistent with the modeling results of Melnick et al. (2017), who propose elastic bending of both plates as the responsible mechanism. We find that the model result of lateral ELM due to viscous relaxation is caused by the elastic response of the overriding plate to the trenchward flow produced by viscous relaxation in the mantle wedge. We characterize this response as consisting primarily of in-plane bending, in agreement with the inferences of Melnick et al. (2017) and Loveless (2017).

A crucial finding, from a modeling perspective, is that the ELM relies on trench-perpendicular velocity changes being restricted at a certain distance from the trench. The distance between the trench and this restriction determines the spatial pattern and amplitude of landward velocity changes in response to a given earthquake. The model of Melnick et al. (2017) applied this restriction at all depths, in the form of a backstop (free-slip boundary condition on a vertical model boundary), parallel to the trench and located 700 km landward of it. Our models extend for nearly 2000 km landward of the trench and instead rely on the restriction of afterslip above a certain depth (100 km in the reference model). There is no direct evidence of the depth at which variable shear rates cease on the mantle wedge–slab boundary, or even if there is such a depth. Afterslip has been inferred to occur deeper than 40 km, but there is no evidence of it taking place beyond 100 km depth at most (Diao et al., 2014; Freed et al., 2017; Hu, Bürgmann, Uchida, et al., 2016; Sun et al., 2014; Yamagiwa et al., 2015; Klein et al., 2016). It is plausible, although not certain, that substantially deeper afterslip is not only undetectable at the surface, but truly absent because of mechanical coupling between the mantle wedge and slab, in the absence of a localized shear zone. In this case, postseismic viscous relaxation is expected to produce no ELM.

4.2.2 Incompatibility With Observations

The rate of ELM, in our models that produce it, is much smaller than in observations. The observed ELM generally increases with the magnitude of the associated earthquake, as does the ELM in our model. However, the largest observed landward velocity change, following the Tohoku earthquake (M_W 9.1), is more than an order of magnitude greater than in our reference model. This is the case even accounting for the smaller magnitude of the model earthquake (M_W 8.9) and for the linear scaling of modeled ELM with seismic moment M_0. For the smaller earthquakes, the scaling indicates that ELM should be as much as two orders of magnitude smaller (for the Oaxaca earthquake, M_W

7.4). Instead, the observed ELM following those earthquakes is only an order of magnitude smaller than the maximum observed value for the much larger Tohoku-oki event (Yuzariyadi & Heki, 2021). Furthermore, the observed along-trench location of the ELM is also closer to the middle of the rupture than in the reference model, especially after the Iquique, Bengkulu and Oaxaca earthquakes.

Our sensitivity tests indicate that overriding plate rheology and restrictions on afterslip affect the amplitudes and spatial pattern of the velocity changes. In particular, introducing a lateral contrast between a more compliant overriding plate lithosphere (in the arc and backarc) and a less compliant plate interior increases the landward velocity changes. Such a contrast was inferred to determine the localization of high gradients in horizontal interseismic velocities in the arc and backarc, observed in multiple subduction zones (D'Acquisto et al., submitted). It is thus likely that the same compliance contrast responsible for the distribution of interseismic velocities amplifies the ELM produced by viscous relaxation, making it at least partly responsible for the fluctuations in the landward velocity changes observed in the early postseismic transient period.

Decreasing the viscosity in the mantle wedge can also produce large velocity changes, even accounting for the trenchward motion due to afterslip early after the earthquake, but with rapid rates of decay with time. Increasing the viscosity produces a slower rate of decay of the velocity changes. Either way, the results are not consistent with the observations, which show consistently long-lasting landward velocity changes, starting right after the earthquake and stabilizing to values of several $\mathrm{mm} \cdot \mathrm{yr}^{-1}$ after a transient period of a few years, during which afterslip occurs (Yuzariyadi & Heki, 2021). Different rheologies not used in our models, such as Burgers viscoelasticity, could modulate the decay of velocity changes in different ways. For instance, large landward amplitudes could be achieved in the short term while exhibiting long-term viscosities compatible with the geodynamics of subduction zones. However, such rheologies cannot provide both large amplitudes and slow decay to the velocity changes due to relaxation of the same stress changes. Furthermore, the along-trench vicinity to the rupture of the landward velocity changes observed after the Bengkulu, Tokachi-oki and Oaxaca earthquakes cannot be reproduced by any of the models in our sensitivity testing.

We find that afterslip produces entirely trenchward motion of the overriding plate in all our models. This is in contrast with the hypothesis that the bending producing landward velocity changes is driven by afterslip, proposed by Loveless (2017). In our models, afterslip is modeled as instantaneous and viscous relaxation happens after it has finished. Our implementation of the two postseismic relaxation processes in our models captures the main features of interseismic and coseismic behavior and allows to easily distinguish the contribution of afterslip and viscous relaxation. At the same time, it avoids the computational demands and expanded parameter space caused by simulating viscous flow in a narrow channel. However, in reality, afterslip has a finite duration and interacts with bulk viscous flow (Masuti et al., 2016; Muto et al., 2019; Agata et al., 2019; Yamagiwa et al., 2015). The degree to which afterslip affects the observed velocity changes depends on its distribution through time, as well as on the observation period and method of computation of the velocity changes from the displacement time series. The lack of a realistic temporal distribution of afterslip and the resulting surface displacement is a limitation of our implementation and precludes a direct comparison with observed displacement time series. Nevertheless, the entirely trenchward motion due to afterslip implies that the observed trench-perpendicular velocity changes, with amplitudes of several $\mathrm{mm \cdot yr^{-1}}$, cannot be explained by afterslip supplementing the motion due to viscous relaxation. This conclusion should not be affected by the lack of two-way feedback between afterslip and viscous relaxation, as the mechanical interaction between the two postseismic relaxation mechanisms has a small effect on the cumulative amplitude of horizontal displacement and on its spatio-temporal evolution, compared to the two processes not interacting (Muto et al., 2019; Agata et al., 2019).

We find that the modeled velocity changes due to viscous relaxation decay with time as the stresses are relaxed (Fig. 3c). The contribution of afterslip, when distributed in time, must produce a trenchward signal in trench-perpendicular velocity changes. The resulting total velocity change due to both relaxation mechanisms should exhibit highly transient behavior, becoming more landward with time as afterslip decays. It should only reach small values (less than a $\mathrm{mm \cdot yr^{-1}}$ in the reference model) and then decay in time as viscous relaxation continues. A transition from trenchward velocity changes in the first year to landward velocity changes in the second year after the Iquique earthquake is indeed observed by Hoffmann et al. (2018). Yuzariyadi and Heki (2021) observe generally less drastic temporal evolution of the velocity changes for all the six earthquake they consider, including Iquique. However, they only analyze the temporal evolution of velocity changes at one station per earthquake. They do observe a transition from trenchward to landward velocity change in the first and second years, respectively, after the Oaxaca earthquake, at the Puerto Escondido station (OXPE). These transitions likely reflect substantial deep afterslip occurring only shortly after the earthquake, ceasing after about 1 year. Both Hoffmann et al. (2018) and Yuzariyadi and Heki (2021) agree that the velocity changes remain landward after afterslip is inferred to have ceased. No decay in the amplitudes of the trench-perpendicular velocity changes is observed by Yuzariyadi and Heki (2021) after the transient period. Amplitudes are constant after 2 years, except for a slight decay up to 5 years after the Tohoku earthquake and for a moderate increase up to 5 years after the Iquique earthquake. The two longest sets of time series, after the Tohoku and Tokachi earthquakes, show constant velocity changes in the last 4 years. This lack of decay cannot be explained by postseismic relaxation in our models.

Overall, we find that the elastic response of the plate to viscous relaxation, proposed by Melnick et al. (2017) and Loveless (2017), can plausibly occur, although only if full mechanical coupling between the slab and mantle wedge is assumed to occur at a certain depth. We confirm that this response consists primarily of in-plane bending caused by the trenchward flow in the mantle wedge during viscous relaxation. However, according to our simulations, it is extremely unlikely that the temporal and spatial pattern of observed landward velocity changes later described by Yuzariyadi and Heki (2021) is primarily produced by bending in response to postseismic relaxation.

4.3 Seismic Hazard Implications

If the observed velocity changes are not attributable to bending caused by viscous relaxation, they must be caused by other mechanisms. Two have been proposed so far. The first consists of changes in the interplate coupling on the megathrust, specifically an increase in the area of strong coupling (Loveless & Meade, 2016). The second is a transient increase in the velocity of the slab due to the altered force balance caused by the unlocking of the portion of the megathrust ruptured during the earthquake (Heki & Mitsui, 2013). An increased area of coupling is a straightforward possible interpretation for any landward change in velocity at subduction zones. However, no explanation has been proposed for a megathrust earthquake rupture causing friction increases hundreds of km away. Transient slab acceleration, conversely, describes a physical mechanism. Yuzariyadi and Heki (2021) test the correlations between velocity changes and earthquake features predicted by the transient slab acceleration hypothesis for all six events. They find the evidence inconclusive but compatible with the hypothesis. Further research is needed to investigate frictional behavior of the megathrust interface possibly responsible for increased coupling. Future studies should also look for further geodetic evidence of transient slab acceleration, including elsewhere in the megathrust subduction system.

Both increased coupling and slab acceleration invoke an increased slip deficit under the lateral areas where the ELM is detected, although for different reasons. Therefore, regardless of which of the two explanations is correct, it is likely that the seismic hazard increases at the locations and time at which enhanced landward velocities are observed. Discriminating between the two mechanism is also needed to distinguish whether the increased hazard consists of a greater likelihood of rupture (implied by greater stressing rate due to slab acceleration) or greater peak slip during the future ruptures.

5 Conclusions

Viscous relaxation can indeed produce ELM. The mechanism producing ELM is the elastic, in-plane response of the overriding plate to the trenchward viscous flow due to relaxation in the mantle wedge. This elastic response consists largely of in-plane elastic bending of the plate. This mechanism relies on the restriction of afterslip provided by the mechanical coupling of the mantle wedge and slab beyond the maximum depth of afterslip. Coupling of the megathrust in the lateral portions of the megathrust, above which ELM is observed, is not needed, nor interferes significnatly, with the production of ELM by postseismic viscous relaxation.

Enhanced landward velocity changes due to postseismic relaxation are expected to be small compared to observations. They also exhibit transient behavior inconsistent with observations. Furthermore, expected ELM is restricted to greater along-trench distances from the rupture than observed. We conclude that it is likely that the observed ELM is not explained by the postseismic plate bending. The most plausible explanation is thus that slip deficit accumulates at greater rates at the locations and times at which lateral landward velocity changes are observed, increasing seismic hazard there and then. The acting mechanism and the specific seismic hazard changes it implies remain to be clarified.

6 Acknowledgements

We wish to thank the anonymous reviewer #3 of a previously submitted manuscript. The reviewer's comments and constructive criticism were instrumental in prompting us to reevaluate key parts of our methodology and conclusions.

Author contributions following the CReDiT taxonomy: Conceptualization: R. Govers; Data curation: M. D'Acquisto; Formal analysis: M. D'Acquisto; Funding acquisition: R. Govers; Investigation: M. D'Acquisto; Methodology: R. Govers, M. W. Herman; Project administration: R. Govers; Resources: R. Govers; Software: R. Govers, M. W. Herman; Supervision: R. Govers, R. M. A. Riva; Validation: M. D'Acquisto; Visualization: M. D'Acquisto; Writing - original draft: M. D'Acquisto, R. Govers, R. M. A. Riva; Writing- review and editing;

Input and output files and the software source codes that were used for the models of this paper will be available in the FAIR-compliant Yoda repository of Utrecht University at the time of publication.

Finite element meshes for the models in this paper are generated using Gmsh (Geuzaine & Remacle, 2009). Figures are made using Generic Mapping Tools (GMT) (version 6.3, Wessel et al., 2019) and Adobe Illustrator (Adobe Inc., 2019).

M.D. was funded by Dutch Research Council (NWO) grant ALWGO.2017.007.

References

Adobe Inc. (2019). *Adobe Illustrator.*

Agata, R., Barbot, S. D., Fujita, K., Hyodo, M., Iinuma, T., Nakata, R., ... Hori, T. (2019). Rapid mantle flow with power-law creep explains deformation after the 2011 Tohoku mega-quake. *Nature Communications*, *10*(1), 1–11. doi: 10.1038/s41467-019-08984-7

Azúa, B. M., DeMets, C., & Masterlark, T. (2002). Strong interseismic coupling, fault afterslip, and viscoelastic flow before and after the Oct. 9, 1995 Colima-Jalisco earthquake: Continuous GPS measurements from Colima, Mexico. *Geophysical Research Letters*, *29*(8), 122-1-122-4. doi: 10.1029/2002GL014702

Balay, S., Abhyankar, S., Adams, M. F., Benson, S., Brown, J., Brune, P., ... Zhang, J. (2021a). *PETSc/TAO users manual* (Tech. Rep. No. ANL-21/39 -

Revision 3.16). Argonne National Laboratory.

Balay, S., Abhyankar, S., Adams, M. F., Benson, S., Brown, J., Brune, P., ... Zhang, J. (2021b). *PETSc Web page.* https://petsc.org/.

Balay, S., Gropp, W. D., McInnes, L. C., & Smith, B. F. (1997). Efficient management of parallelism in object oriented numerical software libraries. In E. Arge, A. M. Bruaset, & H. P. Langtangen (Eds.), *Modern software tools in scientific computing* (pp. 163–202). Birkhäuser Press.

Behr, W. M., & Bürgmann, R. (2020). *What's down there? The structures, materials and environment of deep-seated tremor and slip* (Preprint). EarthArXiv. doi: 10.31223/osf.io/tyzb9

Bürgmann, R., & Dresen, G. (2008). Rheology of the Lower Crust and Upper Mantle: Evidence from Rock Mechanics, Geodesy, and Field Observations. *Annual Review of Earth and Planetary Sciences*, *36*(1), 531–567. doi: 10.1146/annurev.earth.36.031207.124326

Chlieh, M., Avouac, J. P., Sieh, K., Natawidjaja, D. H., & Galetzka, J. (2008). Heterogeneous coupling of the Sumatran megathrust constrained by geodetic and paleogeodetic measurements. *Journal of Geophysical Research: Solid Earth*, *113*(B5). doi: 10.1029/2007JB004981

Diao, F., Xiong, X., Wang, R., Zheng, Y., Walter, T. R., Weng, H., & Li, J. (2014). Overlapping post-seismic deformation processes: Afterslip and viscoelastic relaxation following the 2011 Mw 9.0 Tohoku (Japan) earthquake. *Geophysical Journal International*, *196*(1), 218–229. doi: 10.1093/gji/ggt376

Dziewonski, A. M. (1984). Mapping the lower mantle: Determination of lateral heterogeneity in P velocity up to degree and order 6. *Journal of Geophysical Research: Solid Earth*, *89*(B7), 5929–5952. doi: 10.1029/JB089iB07p05929

Dziewonski, A. M., & Anderson, D. L. (1981). Preliminary reference Earth model. *Physics of the Earth and Planetary Interiors*, *25*(4), 297–356. doi: 10.1016/0031-9201(81)90046-7

Fletcher, R. (1988). *Practical Methods of Optimization.* Wiley.

Freed, A. M., Hashima, A., Becker, T. W., Okaya, D. A., Sato, H., & Hatanaka, Y. (2017). Resolving depth-dependent subduction zone viscosity and afterslip from postseismic displacements following the 2011 Tohoku-oki, Japan earthquake. *Earth and Planetary Science Letters*, *459*, 279–290. doi:

10.1016/j.epsl.2016.11.040

Fujiwara, T., Kodaira, S., No, T., Kaiho, Y., Takahashi, N., & Kaneda, Y. (2011). The 2011 Tohoku-Oki Earthquake: Displacement Reaching the Trench Axis. *Science*, *334*(6060), 1240–1240. doi: 10.1126/science.1211554

Gabriel, E., Fagg, G. E., Bosilca, G., Angskun, T., Dongarra, J. J., Squyres, J. M., ... Woodall, T. S. (2004). Open MPI: Goals, Concept, and Design of a Next Generation MPI Implementation. In D. Hutchison et al. (Eds.), *Recent Advances in Parallel Virtual Machine and Message Passing Interface* (Vol. 3241, pp. 97–104). Berlin, Heidelberg: Springer Berlin Heidelberg. doi: 10.1007/978-3-540-30218-6_19

Geuzaine, C., & Remacle, J.-F. (2009). Gmsh: A 3-D finite element mesh generator with built-in pre- and post-processing facilities. *International Journal for Numerical Methods in Engineering*, *79*(11), 1309–1331. doi: 10.1002/nme.2579

Govers, R., Furlong, K. P., van de Wiel, L., Herman, M. W., & Broerse, T. (2018). The Geodetic Signature of the Earthquake Cycle at Subduction Zones: Model Constraints on the Deep Processes. *Reviews of Geophysics*, *56*(1), 6–49. doi: 10.1002/2017RG000586

Govers, R., & Meijer, P. T. (2001). On the dynamics of the Juan de Fuca plate. *Earth and Planetary Science Letters*, *189*(3), 115–131. doi: 10.1016/S0012-821X(01)00360-0

Govers, R., & Wortel, M. J. R. (1993). Initiation of asymmetric extension in continental lithosphere. *Tectonophysics*, *223*(1), 75–96. doi: 10.1016/0040-1951(93)90159-H

Govers, R., & Wortel, M. J. R. (2005). Lithosphere tearing at STEP faults: Response to edges of subduction zones. *Earth and Planetary Science Letters*, *236*(1), 505–523. doi: 10.1016/j.epsl.2005.03.022

Hardebeck, J. L. (2015). Stress orientations in subduction zones and the strength of subduction megathrust faults. *Science*, *349*(6253), 1213–1216. doi: 10.1126/science.aac5625

Hayes, G. P., Moore, G. L., Portner, D. E., Hearne, M., Flamme, H., Furtney, M., & Smoczyk, G. M. (2018). Slab2, a comprehensive subduction zone geometry model. *Science*, *362*(6410), 58–61. doi: 10.1126/science.aat4723

Heki, K., & Mitsui, Y. (2013). Accelerated pacific plate subduction following interplate thrust earthquakes at the Japan trench. *Earth and Planetary Science Letters*, *363*, 44–49. doi: 10.1016/j.epsl.2012.12.031

Herman, M. W., Furlong, K. P., & Govers, R. (2018). The Accumulation of Slip Deficit in Subduction Zones in the Absence of Mechanical Coupling: Implications for the Behavior of Megathrust Earthquakes. *Journal of Geophysical Research: Solid Earth*, *123*(9), 8260–8278. doi: 10.1029/2018JB016336

Herman, M. W., & Govers, R. (2020). Locating Fully Locked Asperities Along the South America Subduction Megathrust: A New Physical Interseismic Inversion Approach in a Bayesian Framework. *Geochemistry, Geophysics, Geosystems*, *21*(8), e2020GC009063. doi: 10.1029/2020GC009063

Hoffmann, F., Metzger, S., Moreno, M., Deng, Z., Sippl, C., Ortega-Culaciati, F., & Oncken, O. (2018). Characterizing Afterslip and Ground Displacement Rate Increase Following the 2014 Iquique-Pisagua Mw 8.1 Earthquake, Northern Chile. *Journal of Geophysical Research: Solid Earth*, *123*(5), 4171–4192. doi: 10.1002/2017JB014970

Hu, Y., Bürgmann, R., Banerjee, P., Feng, L., Hill, E. M., Ito, T., … Wang, K. (2016). Asthenosphere rheology inferred from observations of the 2012 Indian Ocean earthquake. *Nature*, *538*(7625), 368–372. doi: 10.1038/nature19787

Hu, Y., Bürgmann, R., Uchida, N., Banerjee, P., & Freymueller, J. T. (2016). Stress-driven relaxation of heterogeneous upper mantle and time-dependent afterslip following the 2011 Tohoku earthquake. *Journal of Geophysical Research: Solid Earth*, *121*(1), 385–411. doi: 10.1002/2015JB012508

Ikari, M. J., Marone, C., & Saffer, D. M. (2011). On the relation between fault strength and frictional stability. *Geology*, *39*(1), 83–86. doi: 10.1130/G31416.1

Kanamori, H. (1972). Mechanism of tsunami earthquakes. *Physics of the Earth and Planetary Interiors*, *6*(5), 346–359. doi: 10.1016/0031-9201(72)90058-1

Kawakatsu, H., Kumar, P., Takei, Y., Shinohara, M., Kanazawa, T., Araki, E., & Suyehiro, K. (2009). Seismic Evidence for Sharp Lithosphere-Asthenosphere Boundaries of Oceanic Plates. *Science*, *324*(5926), 499–502. doi: 10.1126/science.1169499

Klein, E., Fleitout, L., Vigny, C., & Garaud, J. (2016). Afterslip and viscoelastic relaxation model inferred from the large-scale post-seismic deformation following the 2010 Mw 8.8 Maule earthquake (Chile). *Geophysical Journal International*, *205*(3), 1455–1472. doi: 10.1093/gji/ggw086

Kumar, P., & Kawakatsu, H. (2011). Imaging the seismic lithosphere-asthenosphere boundary of the oceanic plate. *Geochemistry, Geophysics, Geosystems*, *12*(1). doi: 10.1029/2010GC003358

Landau, L. D., Lifshitz, E. M., Kosevich, A. M., & Pitaevskii, L. P. (1986). *Theory of Elasticity* (Third ed., Vol. 7). Elsevier Butterworth Heinemann.

Lay, T., Kanamori, H., Ammon, C. J., Koper, K. D., Hutko, A. R., Ye, L., … Rushing, T. M. (2012). Depth-varying rupture properties of subduction zone megathrust faults. *Journal of Geophysical Research: Solid Earth*, *117*(B4). doi: 10.1029/2011JB009133

Lindsey, E. O., Mallick, R., Hubbard, J. A., Bradley, K. E., Almeida, R. V., Moore, J. D. P., … Hill, E. M. (2021). Slip rate deficit and earthquake potential on shallow megathrusts. *Nature Geoscience*, *14*(5), 321–326. doi: 10.1038/s41561-021-00736-x

Liu, X., Zhao, D., Li, S., & Wei, W. (2017). Age of the subducting Pacific slab beneath East Asia and its geodynamic implications. *Earth and Planetary Science Letters*, *464*, 166–174. doi: 10.1016/j.epsl.2017.02.024

Loveless, J. P. (2017). Super-interseismic periods: Redefining earthquake recurrence: Super-interseismic Periods. *Geophysical Research Letters*, *44*(3), 1329–1332. doi: 10.1002/2017GL072525

Loveless, J. P., & Meade, B. J. (2010). Geodetic imaging of plate motions, slip rates, and partitioning of deformation in Japan. *Journal of Geophysical Research*, *115*(B2), B02410. doi: 10.1029/2008JB006248

Loveless, J. P., & Meade, B. J. (2011). Spatial correlation of interseismic coupling and coseismic rupture extent of the 2011 MW = 9.0 Tohoku-oki earthquake. *Geophysical Research Letters*, *38*(17). doi: 10.1029/2011GL048561

Loveless, J. P., & Meade, B. J. (2016). Two decades of spatiotemporal variations in subduction zone coupling offshore Japan. *Earth and Planetary Science Letters*, *436*, 19–30. doi: 10.1016/j.epsl.2015.12.033

Masuti, S., Barbot, S. D., Karato, S.-i., Feng, L., & Banerjee, P. (2016). Upper-mantle water stratification inferred from observations of the 2012 Indian Ocean earthquake. *Nature*, *538*(7625), 373–377. doi: 10.1038/nature19783

Mavrommatis, A. P., Segall, P., & Johnson, K. M. (2014). A decadal-scale deformation transient prior to the 2011 M_w 9.0 Tohoku-oki earthquake. *Geophysical Research Letters*, *41*(13), 4486–4494. doi: 10.1002/2014GL060139

Melnick, D., Moreno, M., Quinteros, J., Baez, J. C., Deng, Z., Li, S., & Oncken, O. (2017). The super-interseismic phase of the megathrust earthquake cycle in Chile: The Super-interseismic Earthquake Cycle. *Geophysical Research Letters*, *44*(2), 784–791. doi: 10.1002/2016GL071845

Melosh, H. J., & Raefsky, A. (1981). A simple and efficient method for introducing faults into finite element computations. *Bulletin of the Seismological Society of America*, *71*(5), 1391–1400. doi: 10.1785/BSSA0710051391

Melosh, H. J., & Raefsky, A. (1983). Anelastic response of the Earth to a dip slip earthquake. *Journal of Geophysical Research: Solid Earth*, *88*(B1), 515–526. doi: 10.1029/JB088iB01p00515

Melosh, H. J., & Williams, C. A. (1989). Mechanics of graben formation in crustal rocks: A finite element analysis. *Journal of Geophysical Research: Solid Earth*, *94*(B10), 13961–13973. doi: 10.1029/JB094iB10p13961

Meltzner, A. J., Sieh, K., Chiang, H.-W., Wu, C.-C., Tsang, L. L. H., Shen, C.-C., … Briggs, R. W. (2015). Time-varying interseismic strain rates and similar seismic ruptures on the Nias–Simeulue patch of the Sunda megathrust. *Quaternary Science Reviews*, *122*, 258–281. doi: 10.1016/j.quascirev.2015.06.003

Métois, M., Socquet, A., & Vigny, C. (2012). Interseismic coupling, segmentation and mechanical behavior of the central Chile subduction zone. *Journal of Geophysical Research: Solid Earth*, *117*(B3). doi: 10.1029/2011JB008736

Moore, J. C., & Saffer, D. (2001). Updip limit of the seismogenic zone beneath the accretionary prism of southwest Japan: An effect of diagenetic to low-grade metamorphic processes and increasing effective stress. *Geology*, *29*(2), 183–186. doi: 10.1130/0091-7613(2001)029⟨0183:ULOTSZ⟩2.0.CO;2

Moreno, M., Melnick, D., Rosenau, M., Bolte, J., Klotz, J., Echtler, H., … Oncken, O. (2011). Heterogeneous plate locking in the South–Central Chile subduction zone: Building up the next great earthquake. *Earth and Planetary Science Letters*, *305*(3), 413–424. doi: 10.1016/j.epsl.2011.03.025

Muto, J., Moore, J. D. P., Barbot, S., Iinuma, T., Ohta, Y., & Iwamori, H. (2019). Coupled afterslip and transient mantle flow after the 2011 Tohoku earthquake.

Science Advances, *5*(9), eaaw1164. doi: 10.1126/sciadv.aaw1164

Ozawa, S., Kaidzu, M., Murakami, M., Imakiire, T., & Hatanaka, Y. (2004). Coseismic and postseismic crustal deformation after the M_ω 8 Tokachi-oki earthquake in Japan. *Earth, Planets and Space*, *56*(7), 675–680. doi: 10.1186/BF03352530

Ozawa, S., Nishimura, T., Suito, H., Kobayashi, T., Tobita, M., & Imakiire, T. (2011). Coseismic and postseismic slip of the 2011 magnitude-9 Tohoku-Oki earthquake. *Nature*, *475*(7356), 373–376. doi: 10.1038/nature10227

Perfettini, H., & Avouac, J.-P. (2004). Stress transfer and strain rate variations during the seismic cycle. *Journal of Geophysical Research: Solid Earth*, *109*(B6). doi: 10.1029/2003JB002917

Philibosian, B., Sieh, K., Avouac, J.-P., Natawidjaja, D. H., Chiang, H.-W., Wu, C.-C., ... Suwargadi, B. W. (2014). Rupture and variable coupling behavior of the Mentawai segment of the Sunda megathrust during the supercycle culmination of 1797 to 1833. *Journal of Geophysical Research: Solid Earth*, *119*(9), 7258–7287. doi: 10.1002/2014JB011200

Plafker, G. (1972). Alaskan earthquake of 1964 and Chilean earthquake of 1960: Implications for arc tectonics. *Journal of Geophysical Research (1896-1977)*, *77*(5), 901–925. doi: 10.1029/JB077i005p00901

Protti, M., González, V., Newman, A. V., Dixon, T. H., Schwartz, S. Y., Marshall, J. S., ... Owen, S. E. (2014). Nicoya earthquake rupture anticipated by geodetic measurement of the locked plate interface. *Nature Geoscience*, *7*(2), 117–121. doi: 10.1038/ngeo2038

Ruegg, J. C., Rudloff, A., Vigny, C., Madariaga, R., de Chabalier, J. B., Campos, J., ... Dimitrov, D. (2009). Interseismic strain accumulation measured by GPS in the seismic gap between Constitución and Concepción in Chile. *Physics of the Earth and Planetary Interiors*, *175*(1), 78–85. doi: 10.1016/j.pepi.2008.02.015

Savage, J. C. (1983). A dislocation model of strain accumulation and release at a subduction zone. *Journal of Geophysical Research: Solid Earth*, *88*(B6), 4984–4996. doi: 10.1029/JB088iB06p04984

Scholz, C. H. (1998). Earthquakes and friction laws. *Nature*, *391*(6662), 37–42. doi: 10.1038/34097

Shimazaki, K., & Nakata, T. (1980). Time-predictable recurrence model for large earthquakes. *Geophysical Research Letters*, *7*(4), 279–282. doi: 10.1029/GL007i004p00279

Sladen, A., & Trevisan, J. (2018). Shallow megathrust earthquake ruptures betrayed by their outer-trench aftershocks signature. *Earth and Planetary Science Letters*, *483*, 105–113. doi: 10.1016/j.epsl.2017.12.006

Spence, D. A., Turcotte, D. L., & Stewartson, K. (1979). Viscoelastic relaxation of cyclic displacements on the San Andreas Fault. *Proceedings of the Royal Society of London. A. Mathematical and Physical Sciences*, *365*(1720), 121–144. doi: 10.1098/rspa.1979.0010

Sun, T., Wang, K., Iinuma, T., Hino, R., He, J., Fujimoto, H., ... Hu, Y. (2014). Prevalence of viscoelastic relaxation after the 2011 Tohoku-oki earthquake. *Nature*, *514*(7520), 84–87. doi: 10.1038/nature13778

Tichelaar, B. W., & Ruff, L. J. (1993). Depth of seismic coupling along subduction zones. *Journal of Geophysical Research: Solid Earth*, *98*(B2), 2017–2037. doi: 10.1029/92JB02045

Tomita, F., Kido, M., Osada, Y., Hino, R., Ohta, Y., & Iinuma, T. (2015). First measurement of the displacement rate of the Pacific Plate near the Japan Trench after the 2011 Tohoku-Oki earthquake using GPS/acoustic technique. *Geophysical Research Letters*, *42*(20), 8391–8397. doi: 10.1002/2015GL065746

van Keken, P. E., Kiefer, B., & Peacock, S. M. (2002). High-resolution models of subduction zones: Implications for mineral dehydration reactions and the transport of water into the deep mantle. *Geochemistry, Geophysics, Geosystems*, *3*(10), 1 of 20-20 of 20. doi: 10.1029/2001GC000256

Verfürth, R. (1994). A posteriori error estimation and adaptive mesh-refinement techniques. *Journal of Computational and Applied Mathematics*, *50*(1), 67–83. doi: 10.1016/0377-0427(94)90290-9

Weiss, J. R., Brooks, B. A., Foster, J. H., Bevis, M., Echalar, A., Caccamise, D., ... Vergani, G. (2016). Isolating active orogenic wedge deformation in the southern Subandes of Bolivia. *Journal of Geophysical Research: Solid Earth*, *121*(8), 6192–6218. doi: 10.1002/2016JB013145

Wessel, P., Luis, J. F., Uieda, L., Scharroo, R., Wobbe, F., Smith, W. H. F., & Tian, D. (2019). The Generic Mapping Tools Version 6. *Geochemistry, Geophysics,* *Geosystems*, *20*(11), 5556–5564. doi: 10.1029/2019GC008515

Yamagiwa, S., Miyazaki, S., Hirahara, K., & Fukahata, Y. (2015). Afterslip and viscoelastic relaxation following the 2011 Tohoku-oki earthquake (M_w 9.0) inferred from inland GPS and seafloor GPS/Acoustic data. *Geophysical Research Letters*, *42*(1), 66–73. doi: 10.1002/2014GL061735

Yuzariyadi, M., & Heki, K. (2021). Enhancement of interplate coupling in adjacent segments after recent megathrust earthquakes. *Tectonophysics*, 228719. doi: 10.1016/j.tecto.2021.228719